

Climatic pacing of extreme Nile floods during the North African Humid Period

Received: 6 November 2023

Accepted: 22 May 2024

Published online: 3 July 2024

 Check for updates

Cécile L. Blanchet^{1,6}✉, Arne Ramisch^{1,7}, Rik Tjallingii¹, Monica Ionita^{2,3},
Louison Laruelle^{1,8}, Meike Bagge^{1,9}, Volker Klemann⁴ & Achim Brauer^{1,5}

Understanding how large river systems will respond to an invigorated hydrological cycle as simulated under higher global temperatures is a pressing issue. Insights can be gained from studying past wetter-than-present intervals, such as the North African Humid Period during the early Holocene Epoch (~11–6 thousand years ago). Here we present a 1,500-year-long annually laminated (varved) offshore sediment record that tracks the seasonal discharge of the Nile River during the North African Humid Period. The record reveals mobilization of large amounts of sediments during strong summer floods that may have rendered the Nile valley uninhabitable. More frequent and rapid transitions between extremely strong and weak floods between 9.2 and 8.6 thousand years ago indicate highly instable fluvial dynamics. Climate simulations suggest flood variability was paced by El Niño/Southern Oscillation on interannual timescales, while multi-decadal oscillatory modes drove changes in extreme flood events. These pacemakers have also been identified in the Nile flow records from the Common Era, which implies their stationarity under contrasting hydroclimatic conditions.

The Nile River is an iconic waterway that connects the humid tropics of Africa to the semi-arid Mediterranean coast and has sustained the establishment of complex societies for many millennia¹. Today, the Nile discharge is controlled mainly by seasonal migrations of the African summer monsoon, bringing high amounts of rainfall to the Ethiopian Highlands². Recent episodes of droughts and floods bear serious consequences for communities living in densely populated areas along the Nile course^{3,4}. Global climate models participating in the Coupled Model Intercomparison Project (CMIP) forecast wetter conditions in eastern Africa as well as strongly variable and intermittent Nile river run-off⁵ (Extended Data Fig. 1 and Extended Data Table 1). The combination of higher discharge and more-variable Nile floods poses serious challenges

for water management (storage and distribution) and social stability⁶. However, the model simulations of the Nile response to global warming show a wide range of possible scenarios⁵, leading to highly uncertain forecasts and risks assessment for potential adaptation measures.

To test model simulations and evaluate the response of the Nile River to wetter conditions, we used an annually resolved sediment archive from offshore the Nile mouth deposited during the early Holocene ‘North African Humid Period’ (NAHP)⁷. This period provides useful benchmarks for future climates because it is characterized by a large increase in rainfall in northeastern (NE) Africa (Fig. 1a and Extended Data Figs. 2 and 3) due to stronger insolation and a larger ocean–continent temperature gradient. The estimated amount of rainfall brought

¹Section Landscape Evolution and Climate Dynamics, Helmholtz Centre Potsdam—German Research Centre for Geosciences GFZ, Potsdam, Germany.

²Alfred Wegener Institute Helmholtz Centre for Polar and Marine Research, Bremerhaven, Germany. ³Forest Biometrics Laboratory—Faculty of Forestry, ‘Stefan cel Mare’ University of Suceava, Suceava, Romania. ⁴Section Earth System Modelling, Helmholtz Centre Potsdam—German Research Centre for Geosciences GFZ, Potsdam, Germany. ⁵Institute of Geosciences, University of Potsdam, Potsdam, Germany. ⁶Present address: Section Geomorphology, Helmholtz Centre Potsdam—German Research Centre for Geosciences GFZ, Potsdam, Germany. ⁷Present address: Institute of Geology, University of Innsbruck, Innsbruck, Austria. ⁸Present address: Section Seismic Hazard and Risk Dynamics, Helmholtz Centre Potsdam—German Research Centre for Geosciences GFZ, Potsdam, Germany. ⁹Present address: Federal Institute for Geosciences and Natural Resources, Hannover, Germany.

✉e-mail: blanchet@gfz-potsdam.de

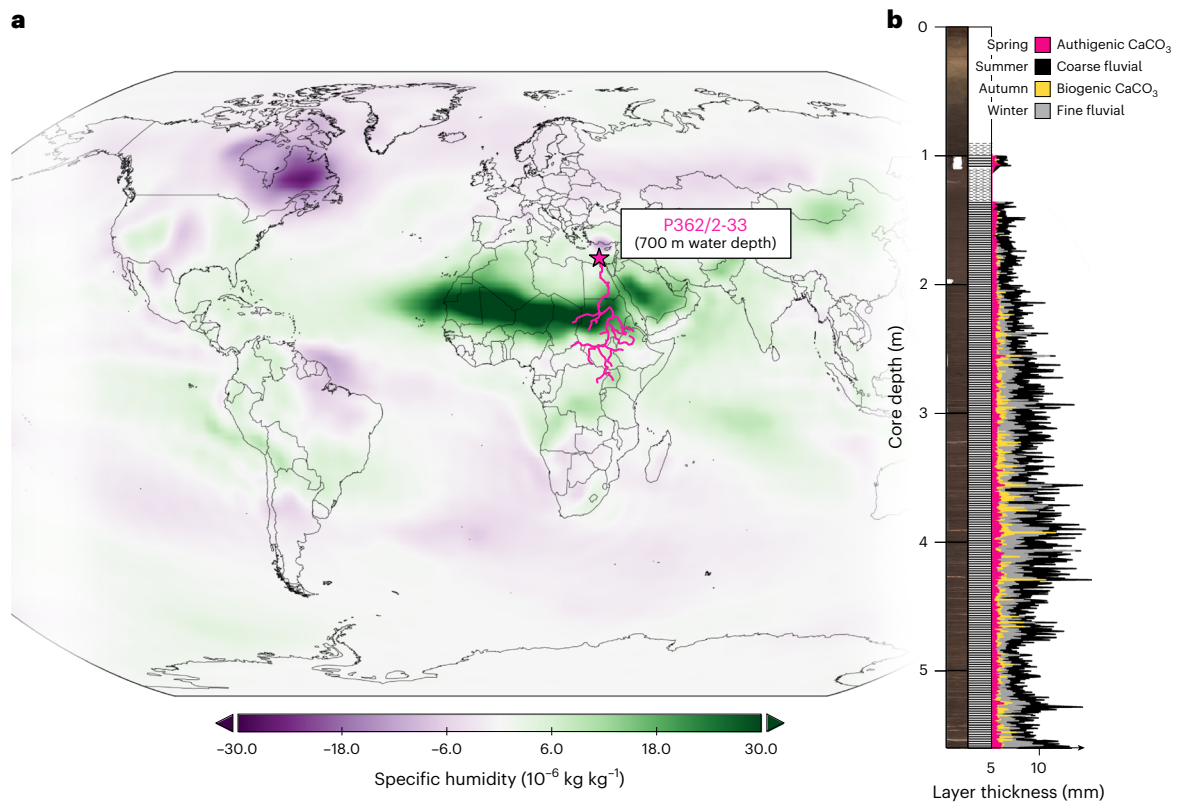


Fig. 1 | Precipitation in the Nile River watershed during the NAHP and varved record of core P362/2-33. a, Map of humidity anomalies at 9 kyr BP (9 K) as compared with pre-industrial conditions estimated by the Alfred Wegener Institute-Earth System Model (AWI-ESM) model (Methods and Extended Data

Figs. 2 and 3), with the Nile River (pink) and the location of core P362/2-33 offshore the mouth of the Nile River (star). **b**, Thickness record of four different sublayers corresponding to seasonal deposits (see legend) along the lithology and photograph of core P362/2-33⁷.

by the monsoon during the NAHP was higher by -75% (refs. 8,9) and is thought to have generated a three- to fivefold increase in Nile River run-off¹⁰. The morphology of the Nile River itself was largely modified, with a dense network of tributaries and a much larger drainage area^{11,12}. Geomorphologic evidence also points to the occurrence of episodes of violent rainfall and torrential floods during the NAHP, which probably led prehistoric populations to abandon the Nile valley¹³⁻¹⁵. So far, the frequency and recurrence of these extreme run-off events have not been examined, which has limited our ability to identify the main driving factors.

Core P362/3-33 is ideally located to record annual changes in Nile flood dynamics during the NAHP (Fig. 1a). This 6-m-long sediment core was retrieved in 2008 on the western Nile deep-sea fan and contains a pristine 5-m-long laminated sequence^{7,16} (Fig. 1b). The chronology was constrained using a combination of radiocarbon dating and annual layer (varve) counting. The radiocarbon ages were obtained on fossil planktic foraminifera *Globigerinoides ruber* (white), which live in subsurface waters and provide a reliable estimation of depositional ages^{7,16}. Varve counting and measurements of sublayer thickness were realized under the microscope. Microfacies analysis revealed a repeating sequence of sublayers that was interpreted as a seasonal depositional cycle⁷, which was used to determine the boundaries of annual layers. The annual deposition of the layers in core P362/3-33 was confirmed by fitting an autoregressive gamma-walk sedimentation model based on a million Monte Carlo simulations through eleven radiocarbon ages (Extended Data Fig. 4). The excellent match between layer thickness expressed as accumulation rates and the probability distribution of radiocarbon ages confirms the presence of varves in core P362/3-33. In addition, this Bayesian model provides us with a very precise and accurate age determination with errors ranging between 90 and 250 years.

A continuous record of summer floods

We obtained a continuous record of -1,500 varves between 9.47 and 7.94 kyr BP. Another 70 varves occur above a non-laminated (bioturbated) interval between 7.69 and 7.62 kyr BP (Fig. 2a). Microfacies analyses identified the flood layers as specific detrital sublayers related to terrestrial sediment-laden hyperpycnal deposits during the annual flood season of the Nile^{7,17}. The flood-layer thickness varies between 0.3 and 10.0 mm, with pronounced changes in the average thickness at -8.08, 8.40, 8.62, 8.80, 8.88, 9.17 and 9.34 kyr BP (± 0.05 kyr) as indicated by change points in the sedimentation model (Fig. 2e and Methods). These changes in flood-layer thickness occur within a few decades (-30–40 years) and indicate large shifts in the volume of sediments deposited on the margin.

At our core site, the annual to centennial variability in flood-layer thicknesses tracks sediment discharge and fluvial activity in the Nile watershed rather than spatial migrations of the depocentre or sea-level changes. The western part of the Nile deep-sea fan is a stable depocentre during the Quaternary period¹⁸ and was particularly active between 15 and 6 kyr BP¹⁹. Local sea-level reconstructions obtained using an ensemble of three-dimensional mantle viscosity structures combined with the ICE-6G glaciation history model for the Nile deep-sea fan show a near-linear rise from about -18 to -2 m between 10 and 8 kyr BP²⁰, with limited glacial isostatic adjustments (Extended Data Fig. 5a). No significant relationship could be observed between flood-layer thickness and rates of sea-level rise during the early Holocene (Extended Data Fig. 5b), which suggests that the post-glacial sea-level rise did not exert a substantial control on sediment dynamics over the western Nile deep-sea fan.

The correlation between flood-layer thickness and particle size provides a solid physical foundation for using our data to reconstruct variations in flood strength (Fig. 2d and Extended Data Fig. 5c,d).

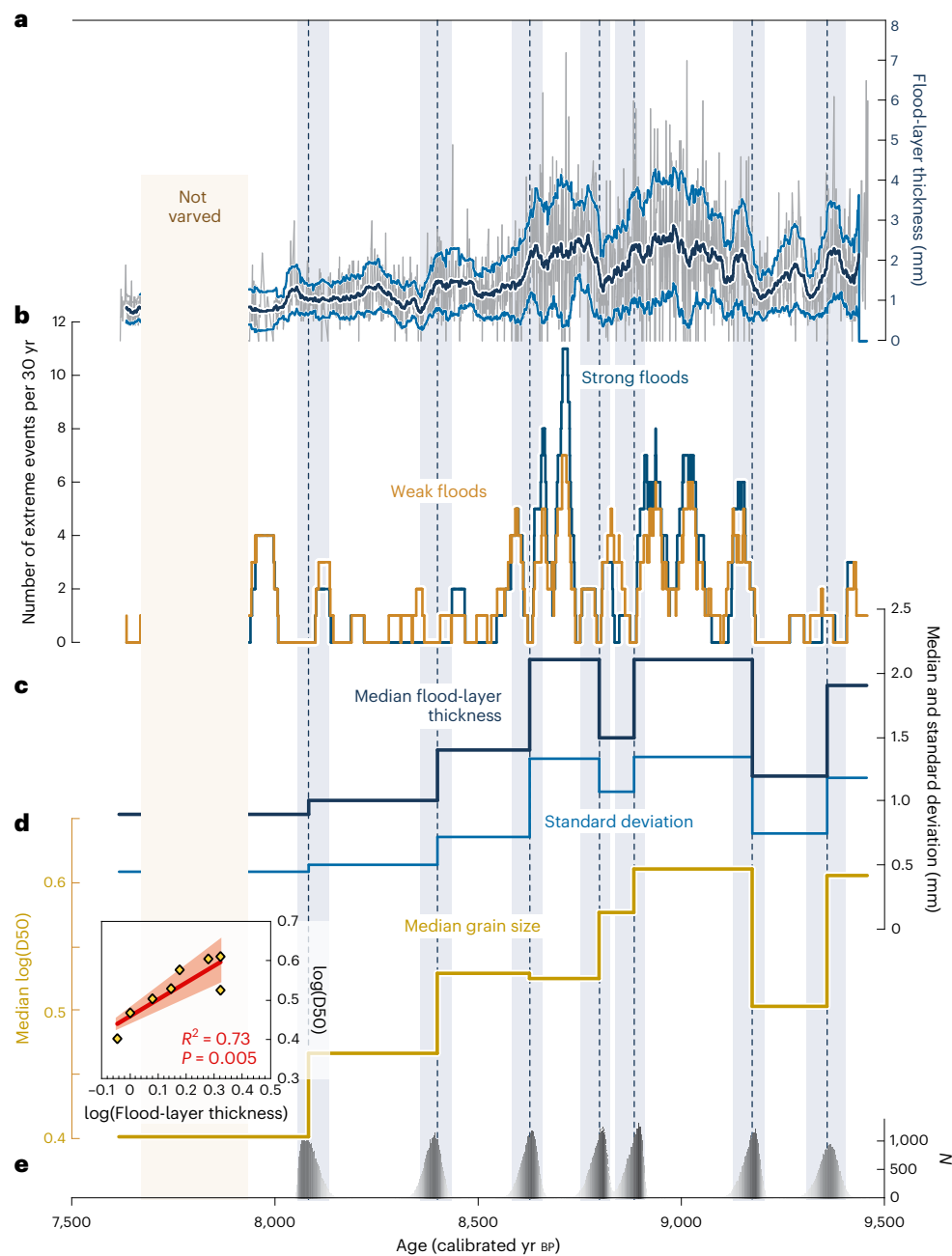


Fig. 2 | Fluvial dynamics of the Nile River during the North African Humid Period (7500–9500 yr BP). **a**, Thickness of flood layers (grey curve), 30-year moving average (dark blue curve) and 2σ confidence (blue curves). **b**, Number of strong and weak floods (respectively, blue and orange curves) per 30 years (Methods and Extended Data Fig. 6). **c**, Median (thick dark blue line) and standard deviation (light blue line) of flood-layer thickness between change points. **d**, Median grain sizes (log(D50), thick gold line) between change points.

e, Change points shown as probability density functions of sedimentation rate (N , number of iterations deviating from a linear accumulation rate), hashed line (median) and grey shading (2σ uncertainty). Insert: relationship between flood-layer thickness and median grain size (bi-plot), which is considered significant since the calculated P value of the null-hypothesis significance test is 0.005. The non-varved part of the record is indicated by a light orange shading and the mention 'Not varved'.

Indeed, the volume of sediment transported by floods might be influenced by complex, nonlinear interactions among rainfall, discharge and sediment availability and mobilization within large river systems. Such complex interactions might lead to heavy rainfall events causing minor erosional episodes, and vice versa^{21,22}. By contrast, the size of particles carried by a stream is directly related to the discharge. This link is well established for the Nile River, where particulate matter during summer floods is predominantly silt-sized, while lower winter flow is characterized by finer, mud-sized particles^{2,23}. The consistent relationship between layer thickness and particle size therefore provides

robust evidence that our record of flood-layer thickness tracks past flood dynamics on interannual to decadal timescales.

Extreme floods and flickering fluvial regimes

The NAHP is characterized by the occurrence of extremely strong and variable Nile floods. In particular, the dominance of thick flood layers between 9.2 and 8.6 kyr BP (Fig. 2a) depicts a period of strong erosional activity in the Nile River basin and the deposition of large amounts of particulate matter offshore. The volume of sediments transported in this time interval was on average two to three times higher than after

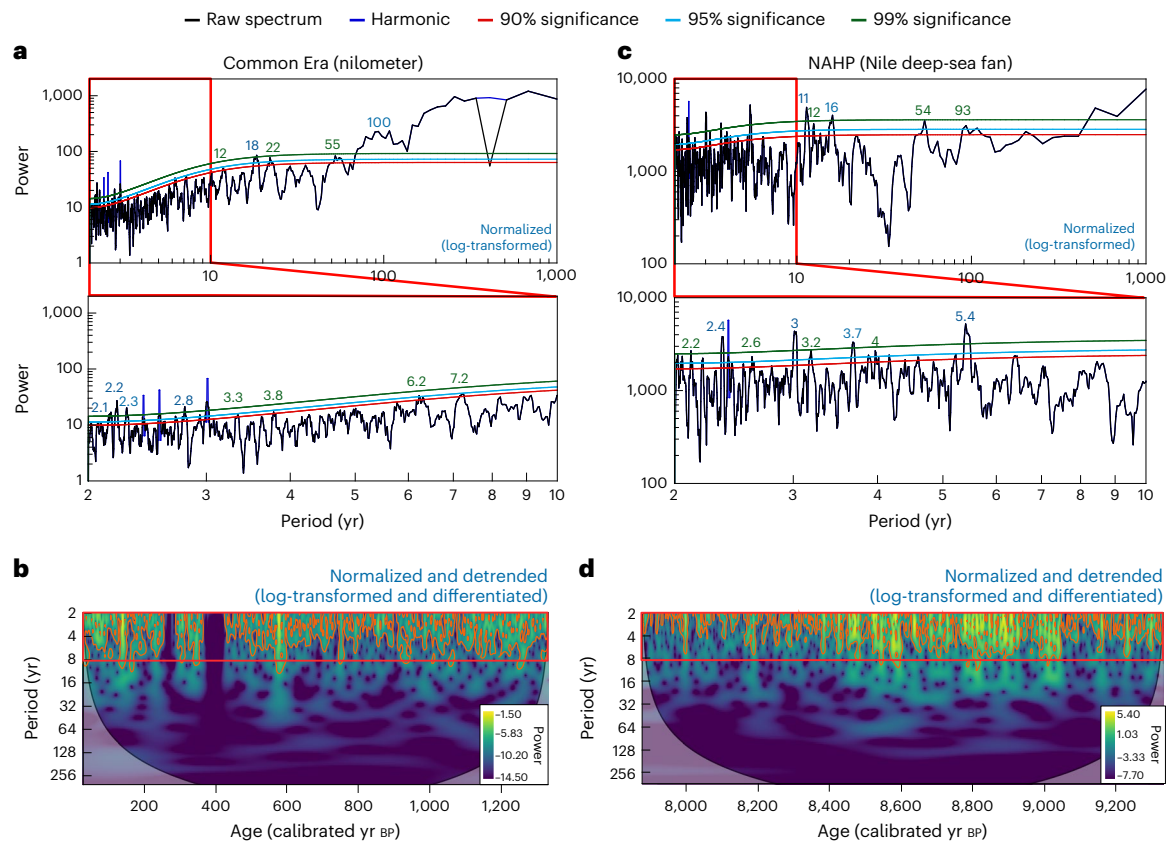


Fig. 3 | Oscillatory regimes during the CE and the NAHP. **a**, Multi-taper analysis of the log-transformed nilometer data with the periodogram (black), harmonics (blue) and significance levels against a red-noise background (90%: red; 95%: light blue; 99%: green). Significant periodicities above the 99% confidence level are indicated in blue and above 95% in green. **b**, Wavelet analyses of the detrended and log-transformed record of high Nile flow from the nilometers³¹ covering the past 1,300 years, with $P = 0.05$ significance levels against a red noise in orange

($\text{lag} = 0.9$), cone of influence overlain. The ENSO band is indicated in the wavelet plots by red rectangles. **c**, Multi-taper analyses of the log-transformed flood thickness record of core P362/2-33 covering the interval 7.5–9.5 kyr BP. **d**, Wavelet analyses of the detrended and log-transformed summer flood thickness record of core P362/3-33. See Methods and Extended Data Figs. 8 and 9 for more details on time-series detrending and normalization.

8.6 kyr BP (Fig. 2c). This order of magnitude is similar to previous estimations of increases in heavy rainfall frequency and Nile run-off during the NAHP^{10,15,24}, suggesting that rainfall intensity might exert a substantial control on the erosional activity in the Nile watershed.

Extreme variations in flood strength during the 9.2–8.6 kyr BP interval is indicated by the much wider variance of flood-layer thickness compared with intervals with lower thickness (Fig. 2c). The frequency of stronger-than-normal and weaker-than-normal floods increases in parallel, although the number of strong floods is generally higher than the number of weak floods (Fig. 2b and Extended Data Fig. 6b,c). Our results suggest that highly erosional periods were associated with increased interannual variability in fluvial dynamics and lend credence to the forecasted stronger Nile flow variance under future warmer and wetter conditions⁵.

Another striking observation is the occurrence of rapid changes in fluvial regime as seen by the existence of change points in the accumulation rates (Fig. 2c and Extended Data Fig. 6e). These changes typically occur within 30–70 years and are characterized by substantial modifications of the erosion regimes in the Nile watershed, leading to the deposition of flood layers with thickness of different median and variance (Fig. 2c). Such rapid switches cannot be readily attributed to a single driver but might result from threshold-like responses of the Nile River to climatic or environmental changes. For example, factors such as changes in moisture source²⁵, vegetation cover²⁶ or fluvial morphology (for example, the activation and abandonments of tributaries)^{11,15} might lead to nonlinear erosional responses. In addition, intervals of stronger volcanic forcing might have triggered Nile flow

failures, especially around 8.9–8.8 and after 8.6 kyr BP^{27,28} (Extended Data Fig. 5e).

Drivers of flood dynamics under intensive rainfall

The occurrence of seasonal floods during the early Holocene has also been reported at onshore locations in the Nile valley, for example, at Lake Faiyum^{29,30}. However, our continuous record of annual Nile floods during the NAHP is unique in the region and allows us to investigate the drivers of interannual hydroclimates under wetter-than-present conditions. In addition, our new NAHP palaeo-flood record is of similar length and resolution as the early Islamic ‘nilometer’ records of past Nile levels at Roda Island (near Cairo) during the Common Era (CE) (622–1922 CE)^{28,31,32}. Therefore, the comparison of flood frequency between these two records helps determine the drivers of flood variability under contrasting hydroclimatic conditions. Once detrended and normalized, the NAHP and CE records were analysed using wavelet and multi-taper methods to detect significant oscillatory regimes (Methods and Extended Data Figs. 7–9)^{31,33}. In both records, a strong signal is found in the interannual range with persistent periodicities between 2 and 7 years (Fig. 3). This oscillatory mode is a clear fingerprint of El Niño/Southern Oscillation (ENSO), which has been shown to drive NE African hydroclimates both at present and during the CE^{31,34,35}. This teleconnection operates through complex ocean–atmosphere interactions that control the zonal moisture (Walker) circulation³⁵. La Niña phases are associated with enhanced rainfall and widespread flooding in the NE African monsoonal realm, while El Niño phases are associated with droughts and negative anomalies of precipitation³⁵.

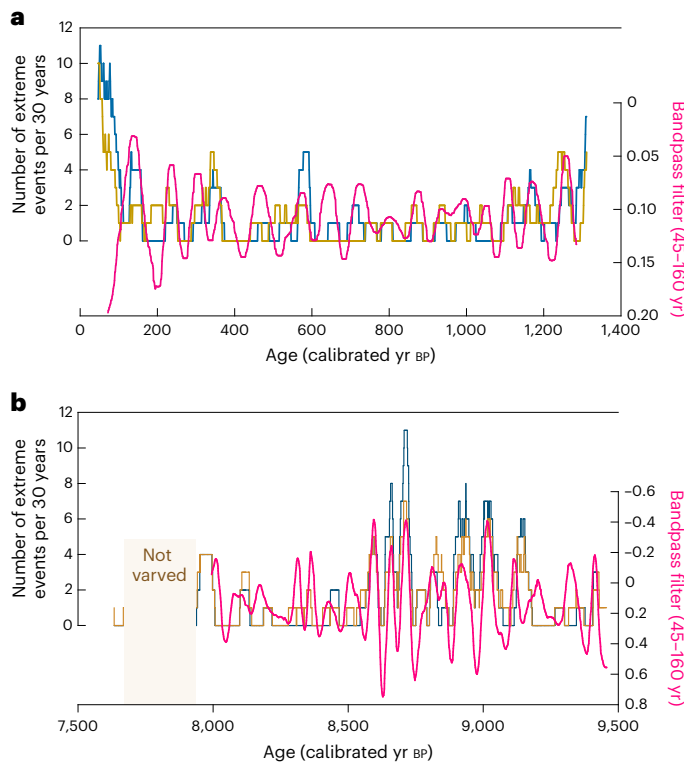


Fig. 4 | Multi-decadal variability drives extreme flood events during the CE and the NAHP. **a**, Number of extreme flood events per 30-year bins (blue: strongest floods; orange: weakest floods) in the high Nile level records (nilometer) during the CE, compared with the filtered log-transformed record of high Nile flood levels (pink). **b**, Similar comparison for the flood thickness record (Nile deep-sea fan) of the NAHP. See Methods for more information on bandpass filtering and data processing; number of extreme floods as in Fig. 2b and Extended Data Figs. 6 and 7.

The identification of the ENSO oscillatory mode in our record of the NAHP demonstrates both the existence of ENSO during the early Holocene and the stationarity of the Pacific–NE Africa teleconnection³⁶. This result provides an important fundament for projections of ENSO-driven climatic and environmental change in a warmer world³⁷.

Recent studies suggested that the spatial pattern of ENSO might have been different during the early Holocene but led to persistent ENSO variability^{38,39}. This finding supports our observations and helps to reconcile contradictory records of past ENSO variability for this time interval^{40–43}. In addition, the spatial characteristics of the so-called ‘coastal’ ENSO dominating the early Holocene is captured in our simulations (Extended Data Fig. 2c)⁴⁴. However, it should be noted that due to higher levels of atmospheric moisture during the early Holocene⁴⁵, even a weak ENSO signal would be amplified and lead to more-variable floods as observed in our record and projected for future climates^{5,46} (Fig. 2c).

Longer, decadal to centennial-scale oscillatory modes are also identified in both CE and NAHP records (Fig. 3). Beyond the periodicities related to the solar cycles (11–22 year sunspot and Hale cycles), two robust periodicities are detected at ~54–55 and 93–100 years, which might be related to the Pacific decadal oscillation⁴⁷ (50–70 years) or the Atlantic multi-decadal oscillation⁴⁸ (40–60 years) (Fig. 3a,c). Although the observed periodicities cannot be attributed to a single climatic mode, their identification provides insights on low-frequency modulation of flood dynamics in the Nile basin. We show that these modes have been operating under contrasting climatic conditions of the CE and NAHP (Fig. 3a,c) and probably modulated the occurrence of flood extremes (Fig. 4). Indeed, bandpass filters applied to the log-transformed flood records show that the number of extreme flood

events is driven largely by multi-decadal oscillations. Despite being widely identified in climate records, the drivers of this multi-decadal variability remain elusive and difficult to capture in global climate models⁴⁹. We show here that in the Nile fluvial system, this variability might be an essential driver of extreme flood events.

In the context of a rapidly changing climate, annually resolved records from past wetter intervals help capture the full range of natural climatic variability in flood records, which is crucial to build reliable forecasting tools⁵⁰. Regular flooding in the Nile River is essential for the subsistence of dense populations in NE Africa but is also the source of important environmental and political pressure (flooding, trans-border conflicts)⁶. We provide here sedimentary evidence of a highly variable river with extremes in flood intensity and strong erosive events during the NAHP. The stationarity of high- and low-frequency signals under contrasting climates of the CE and NAHP provides a strong basis for testing hydrological models incorporating this climatic variability. However, the existence of nonlinearities in the river response to multi-centennial oscillations leading to rapid switches in erosion regime calls for further research. Finally, our data show that the volume of sediments transported and deposited offshore the Nile River varies by a factor 2 to 3 throughout the record. Given that sediment transport is, on interannual to decadal timescales, directly related to river flow, our observations provide relevant benchmarks for scaling future infrastructure.

Online content

Any methods, additional references, Nature Portfolio reporting summaries, source data, extended data, supplementary information, acknowledgements, peer review information; details of author contributions and competing interests; and statements of data and code availability are available at <https://doi.org/10.1038/s41561-024-01471-9>.

References

- Said, R. *The River Nile. Geology, Hydrology and Utilization* (Elsevier, 1993); <https://doi.org/10.1016/C2009-0-11234-5>
- Garzanti, E., Andò, S., Padoan, M., Vezzoli, G. & El Kammar, A. The modern Nile sediment system: processes and products. *Quat. Sci. Rev.* **130**, 9–56 (2015).
- Greater Horn of Africa Climate Risk and Food Security Atlas* (ICPAC, 2018); <https://www.icpac.net/publications/greater-horn-africa-climate-and-food-security-atlas/>
- Wagena, M. B. et al. Climate change in the Blue Nile Basin Ethiopia: implications for water resources and sediment transport. *Clim. Change* **139**, 229–243 (2016).
- Siam, M. S. & Eltahir, E. A. B. Climate change enhances interannual variability of the Nile River flow. *Nat. Clim. Change* **7**, 350–354 (2017).
- Wheeler, K. G., Jeuland, M., Hall, J. W., Zagana, E. & Whittington, D. Understanding and managing new risks on the Nile with the Grand Ethiopian Renaissance Dam. *Nat. Commun.* **11**, 5222 (2020).
- Blanchet, C. L. et al. Deoxygenation dynamics on the western Nile deep-sea fan during sapropel S1 from seasonal to millennial timescales. *Clim. Past* **17**, 1025–1050 (2021).
- Menviel, L. et al. Drivers of the evolution and amplitude of African Humid Periods. *Commun. Earth Environ.* **2**, 237 (2021).
- Chandan, D. & Peltier, W. R. African Humid Period precipitation sustained by robust vegetation, soil, and lake feedbacks. *Geophys. Res. Lett.* **47**, e2020GL088728 (2020).
- Vadsaria, T. et al. Simulating the occurrence of the last sapropel event (S1): Mediterranean basin ocean dynamics simulations using Nd isotopic composition modeling. *Paleoceanogr. Paleoclimatol.* **34**, 237–251 (2019).
- Pachur, H.-J. & Kröpelin, S. Wadi Howar: paleoclimatic evidence from an extinct river system in the southeastern Sahara. *Science* **237**, 298–299 (1987).

12. Williams, M. A. J. Late Pleistocene and Holocene environments in the Nile basin. *Glob. Planet. Change* **69**, 1–15 (2009).
13. Butzer, K. W. in *The Sahara and the Nile* (eds Williams, M. A. J. & Faure, H.) 248–276 (A. A. Balkema, 1979).
14. Kuper, R. & Kröpelin, S. Climate-controlled Holocene occupation in the Sahara: motor of Africa's evolution. *Science* **313**, 803–807 (2006).
15. Zaki, A. S. et al. Did increased flooding during the African Humid Period force migration of modern humans from the Nile Valley? *Quat. Sci. Rev.* **272**, 107200 (2021).
16. Blanchet, C. L. et al. High- and low-latitude forcing of the Nile River regime during the Holocene inferred from laminated sediments of the Nile deep-sea fan. *Earth Planet. Sci. Lett.* **364**, 98–110 (2013).
17. Mologni, C. et al. Frequency of exceptional Nile flood events as an indicator of Holocene hydro-climatic changes in the Ethiopian Highlands. *Quat. Sci. Rev.* **247**, 106543 (2020).
18. Zucker, E., Gvirtzman, Z., Granjeon, D., Garcia-Castellanos, D. & Enzel, Y. The accretion of the Levant continental shelf alongside the Nile Delta by immense margin-parallel sediment transport. *Mar. Pet. Geol.* **126**, 104876 (2021).
19. Hennekam, R., Donders, T. H., Zwiep, K. & de Lange, G. J. Integral view of Holocene precipitation and vegetation changes in the Nile catchment area as inferred from its delta sediments. *Quat. Sci. Rev.* **130**, 189–199 (2015).
20. Bagge, M., Klemann, V., Steinberger, B., Latinović, M. & Thomas, M. Glacial-isostatic adjustment models using geodynamically constrained 3D Earth structures. *Geochem. Geophys. Geosyst.* **22**, e2021GC009853 (2021).
21. Romans, B. W., Castellort, S., Covault, J. A., Fildani, A. & Walsh, J. P. Environmental signal propagation in sedimentary systems across timescales. *Earth Sci. Rev.* **153**, 7–29 (2016).
22. Tofelde, S., Bernhardt, A., Guerit, L. & Romans, B. W. Times associated with source-to-sink propagation of environmental signals during landscape transience. *Front. Earth Sci.* **9**, 227 (2021).
23. Billi, P. & el Badri Ali, O. Sediment transport of the Blue Nile at Khartoum. *Quat. Int.* **226**, 12–22 (2010).
24. Grimm, R. et al. Late glacial initiation of Holocene eastern Mediterranean sapropel formation. *Nat. Commun.* **6**, 7099 (2015).
25. Costa, K., Russell, J., Konecky, B. & Lamb, H. Isotopic reconstruction of the African Humid Period and Congo Air Boundary migration at Lake Tana, Ethiopia. *Quat. Sci. Rev.* **83**, 58–67 (2014).
26. Blanchet, C. L., Frank, M. & Schouten, S. Asynchronous changes in vegetation, runoff and erosion in the Nile River watershed during the Holocene. *PLoS ONE* **9**, e115958 (2014).
27. Paik, S., Min, S.-K., Iles, C. E., Fischer, E. M. & Schurer, A. P. Volcanic-induced global monsoon drying modulated by diverse El Niño responses. *Sci. Adv.* **6**, eaba1212 (2020).
28. Manning, J. G. et al. Volcanic suppression of Nile summer flooding triggers revolt and constrains interstate conflict in ancient Egypt. *Nat. Commun.* **8**, 900 (2017).
29. Marks, L. et al. Holocene lake sediments from the Faiyum Oasis in Egypt: a record of environmental and climate change. *Boreas* **47**, 62–79 (2018).
30. Hamdan, M. A., Flower, R. J., Hassan, F. A. & Hassan, S. M. The Holocene history of the Faiyum Lake (Egypt) based on sediment characteristics, diatoms and ostracods contents. *J. Gt. Lakes Res.* **46**, 456–475 (2020).
31. Kondrashov, D., Feliks, Y. & Ghil, M. Oscillatory modes of extended Nile River records (AD 622–1922). *Geophys. Res. Lett.* **32** (2005).
32. Hassan, F. A. Extreme Nile floods and famines in Medieval Egypt (AD 930–1500) and their climatic implications. *Quat. Int.* **173–174**, 101–112 (2007).
33. Torrence, C. & Webster, P. J. Interdecadal changes in the ENSO–monsoon system. *J. Clim.* **12**, 2679–2690 (1999).
34. Eltahir, E. A. B. & Wang, G. Nilometers, El Niño, and climate variability. *Geophys. Res. Lett.* **26**, 489–492 (1999).
35. Gleixner, S., Keenlyside, N., Viste, E. & Korecha, D. The El Niño effect on Ethiopian summer rainfall. *Clim. Dyn.* **49**, 1865–1883 (2017).
36. McGregor, S., Cassou, C., Kosaka, Y. & Phillips, A. S. Projected ENSO teleconnection changes in CMIP6. *Geophys. Res. Lett.* **49**, e2021GL097511 (2022).
37. Singh, J. et al. Enhanced risk of concurrent regional droughts with increased ENSO variability and warming. *Nat. Clim. Change* **12**, 163–170 (2022).
38. Timmermann, A. et al. El Niño–Southern Oscillation complexity. *Nature* **559**, 535–545 (2018).
39. Karamperidou, C. & DiNezio, P. N. Holocene hydroclimatic variability in the tropical Pacific explained by changing ENSO diversity. *Nat. Commun.* **13**, 7244 (2022).
40. Moy, C. M., Seltzer, G. O., Rodbell, D. T. & Anderson, D. M. Variability of El Niño/Southern Oscillation activity at millennial timescales during the Holocene epoch. *Nature* **420**, 162–165 (2002).
41. Carrè, M., Bentaleb, I., Fontugne, M. & Lavalée, D. Strong El Niño events during the early Holocene: stable isotope evidence from Peruvian sea shells. *Holocene* **15**, 42–47 (2005).
42. Emile-Geay, J. et al. Links between tropical Pacific seasonal, interannual and orbital variability during the Holocene. *Nat. Geosci.* **9**, 168–173 (2016).
43. Lawman, A. E. et al. Unraveling forced responses of extreme El Niño variability over the Holocene. *Sci. Adv.* **8**, eabm4313 (2022).
44. Takahashi, K. & Martínez, A. G. The very strong coastal El Niño in 1925 in the far-eastern Pacific. *Clim. Dyn.* **52**, 7389–7415 (2019).
45. D'Agostino, R., Bader, J., Bordoni, S., Ferreira, D. & Jungclaus, J. Northern Hemisphere monsoon response to mid-Holocene orbital forcing and greenhouse gas-induced global warming. *Geophys. Res. Lett.* **46**, 1591–1601 (2019).
46. Pendergrass, A. G. Changing degree of convective organization as a mechanism for dynamic changes in extreme precipitation. *Curr. Clim. Change Rep.* **6**, 47–54 (2020).
47. Newman, M. et al. The Pacific decadal oscillation, revisited. *J. Clim.* **29**, 4399–4427 (2016).
48. Zhang, R. & Delworth, T. L. Impact of Atlantic multidecadal oscillations on India/Sahel rainfall and Atlantic hurricanes. *Geophys. Res. Lett.* **33** (2006).
49. Mann, M. E., Steinman, B. A. & Miller, S. K. Absence of internal multidecadal and interdecadal oscillations in climate model simulations. *Nat. Commun.* **11**, 49 (2020).
50. Douville, H. et al. in *Climate Change 2021: The Physical Science Basis* (eds Masson-Delmotte, V. et al.) Ch. 8 (Cambridge Univ. Press, 2021).

Publisher's note Springer Nature remains neutral with regard to jurisdictional claims in published maps and institutional affiliations.

Open Access This article is licensed under a Creative Commons Attribution 4.0 International License, which permits use, sharing, adaptation, distribution and reproduction in any medium or format, as long as you give appropriate credit to the original author(s) and the source, provide a link to the Creative Commons licence, and indicate

if changes were made. The images or other third party material in this article are included in the article's Creative Commons licence, unless indicated otherwise in a credit line to the material. If material is not included in the article's Creative Commons licence and your intended use is not permitted by statutory regulation or exceeds the permitted

use, you will need to obtain permission directly from the copyright holder. To view a copy of this licence, visit <http://creativecommons.org/licenses/by/4.0/>.

© The Author(s) 2024

Methods

Microfacies description in core P362/2-33

Core P362/2-33 contains ~5 m of finely laminated sediments that consist of alternating dark- and light-coloured millimetre-thick layers. The microfacies and their chemical composition have been described in detail⁷, and we present here the whole-core thickness measurements for each sublayer type (Fig. 1b). A regular sequence of four types of sublayers occurs throughout the core, with two of them being always present. These sublayers have been associated with seasonal depositional regimes: (1) summer floods, (2) autumn blooms (plankton), (3) winter run-off and (4) authigenic carbonates. Summer flood sublayers are characterized by coarser detrital grains and high Ti/K ratios while winter run-off consists of clay-sized, low Ti/K sediments⁷. Autumn blooms occur after the summer flood and are characterized in core P362/2-33 by the presence of planktic foraminifera shells. Such blooms were observed during historical Nile floods⁵¹. Authigenic carbonates are fine-grained calcite deposits that are interpreted to form in the bottom waters due to anoxic to sulfidic conditions at the end of the spring⁷. Several event layers were also identified in the core as matrix-supported layers and associated with large-scale remobilization episodes or large flood events¹⁷. Their facies is clearly distinct from that of the summer flood sublayers.

The summer flood and winter run-off deposits are the main contributors to the total layer thickness (Fig. 1b). Large changes in the layer thickness of all sublayers are observed throughout the record, with thicker sublayers between -9.2 and 8.7 kyr BP.

Age modelling

To estimate the age–depth relationship in core P362/2-33, we used 11 radiocarbon ages measured on planktic foraminifera *Globigerinoides ruber* that were published in ref. 16. The radiocarbon ages were calibrated using the Marine20 calibration curve, which already contains corrections for reservoir ages⁵².

We constructed the age model using a Bayesian age–depth modelling approach, which leverages relative age information from varve counting as prior information to model absolute age information from radiocarbon dating. The basic aim of this approach is to integrate the two sources of information and obtain a more accurate and precise age–depth relationship. Specifically, we used the varve counts to inform the prior distribution of ages at each depth interval and then updated this distribution using the radiocarbon dating data. By combining these two sources of information, we were able to produce a robust and reliable age–depth model for core P362/2-33.

To incorporate varve counts into a parameterized model for accumulation rates, we employed autoregressive gamma walks, as proposed by ref. 53. The general form of autoregressive gamma walks is given by

$$x_j = \omega x_{j+1} + (1 - \omega) \gamma \quad (1)$$

where x_j is the accumulation rate (in yr cm^{-1}) in depth interval j (with constant spacing Δc), ω is the autocorrelation at lag 1 and γ is a gamma distributed random variable with mean a and shape b ($\gamma \sim \text{Gamma}(a, b)$ iid). To take the pronounced changes in accumulation rates of core P362/2-33 into account, we subdivided the sequence of varve counts into sections with similar mean accumulation rates using the Pruned Exact Linear Time change-point detection algorithm by ref. 54. Subsequently, the three parameters ω_d , a_d and b_d were estimated for each section d . The resulting model was realized 10^6 times and each realization randomly anchored to the probability distribution of the youngest radiocarbon age (Extended Data Fig. 3, light blue area). Subsequently, we updated the ensemble of model realization by selecting age–depth relations maximizing the correspondence to radiocarbon ages (dark blue areas in Extended Data Fig. 4). This optimization process allows us to identify the most probable varve stratigraphy given the absolute age information of radiocarbon dates and quantify the uncertainty in the age estimates.

The modelled age–depth relationship falls within the uncertainty of all the 11 radiocarbon dates (Extended Data Fig. 4). This allows us to build an accurate age model with a high precision (uncertainties are below 100 years) and to maintain the high precision level throughout the profile. The excellent match between accumulation rates derived from varve counting and radiocarbon measurements also confirms the hypothesis that the sequence of four sublayers represents an annual cycle and therefore real varves.

Data analysis

To analyse the data, we used well-established statistical parameters. Following ref. 43, we have calculated the amount of extreme events (high or low flood) per 30 years on both the flood-layer thickness record of core P362/2-33 (Extended Data Fig. 6c) and the nilometer (high Nile) levels (Extended Data Fig. 7c)³¹. However, because our data of flood thickness are constrained (cannot be negative), we have used the log-transformed records and applied a 9 year high-pass filter using the FIR filters in the Past4 software⁵⁵ (Extended Data Figs. 6b and 7b). Extreme events are defined as values higher (lower) than the 95 (5) percentile (Extended Data Figs. 2b and 3b). We then calculated the moving number of extreme high and low floods per 30 year window (Extended Data Figs. 6c and 7c).

Extended Data Fig. 6e shows the distribution of probable ages for the estimated change points ('Age modelling') in the final age model. The histograms represent the number of change points detected by a million Monte Carlo models, which allows us to provide an estimation of uncertainty around each change point and a determination of the skewness of the change-point distribution. The raw flood-layer thicknesses were then split in seven parts between the change points, and the changes in median and standard deviation were calculated (Extended Data Fig. 6d). These analyses show a doubling of the median thickness between different parts of the record, with thicker layers associated with a higher standard deviation than thinner layers.

Glacial isostatic adjustment modelling

We used outputs from the three-dimensional glacial isostatic adjustment model VILMA (Viscoelastic Lithosphere and Mantle Model) to evaluate the changes in relative sea level (RSL) at the core site (29° 50' E, 31° 36' N)²⁰. This model ensemble allows us to test the effect of upper-mantle and asthenosphere viscosity structure on post-glacial sea-level rise according to the ICE-6G glaciation history⁵⁶. The computed RSL variations show a near-linear rise from -18 to -2 m with very little effect of mantle viscosity structures (Extended Data Fig. 5a). After averaging the 18 model outputs (ensemble mean), we calculated the first derivative, which tracks the changes in rates of RSL changes. Finally, we calculated the median values of log-transformed RSL rates between change points to compare them with mean changes in flood-layer thickness (Extended Data Fig. 5b).

Grain-size measurements

The distribution of siliciclastic grains was measured at the University of Innsbruck on a set of 80 samples. After being rinsed three times with ultrapure water (MilliPore system), sediments were decarbonated using buffered acetic acid and the organic matter was removed using concentrated hydrogen peroxide. All solutions were prepared fresh in the clean lab at GFZ Potsdam using ultrapure acids. Samples containing the siliciclastic fraction were then shipped to Innsbruck, where they were mixed with sodium pyrophosphate to avoid the formation of clay aggregates and measured in triplicate on a Malvern Mastersizer 3000.

The results show grain sizes ranging between 0.1 and 100.0 μm with main modes at -0.5–0.6 and 3–4 μm (not shown), very similar to results obtained on this sediment core previously at low resolution¹⁶. For the present study, we report the median grain size (D50), which is modulated by hydrodynamic sorting and flow strength²³. The data are presented as individual samples (Extended Data Fig. 5d) and as

log-transformed averages (median) computed between change points (Extended Data Fig. 5c). Comparing data located in different data spaces (only positive, unconstrained) in a log–log space allows us to compute linear regressions and estimate their statistical significance.

Time-series analysis

To investigate the frequency domain of our annual record of past Nile flow, we applied time-series analyses on the nilometer records of the CE, which are also annually resolved³¹. We present here the multi-taper method results performed on the nilometer and Nile deep-sea fan records using the online SSA-MTM toolkit version 4.4 (ref. 57). The MTM analysis was performed on normalized, log-transformed (log; Extended Data Fig. 8) and differentiated log-transformed ($\log[x_t/x_{t-1}]$) (log(diff); Extended Data Fig. 9) flood-layer thickness and high Nile level data with a resolution of 3 and 5 tapers. The SSA-MTM toolkit allows us to detect harmonics (in blue) and frequencies significant at the 90%, 95% and 99% confidence levels against a red-noise background. These analyses show that both records contain significant frequencies in the range 2–7 years, which is typical of ENSO. The results for the high frequencies (interannual range) are similar for the log and log(diff) data, but the log(diff) spectra are distinctly ‘blue’ (Extended Data Fig. 9a,c) compared with the ‘red’ spectra for log data (Extended Data Fig. 8a,c). This is because the log(diff) procedure filters lower frequencies out of the signal. We therefore favour the log-transformed data for interpreting the MTM spectra (Extended Data Fig. 8a,c).

Another useful method to detect ENSO fingerprints in time series is to apply wavelet analyses³³. We used the software PAST to perform a continuous wavelet transform⁵⁵, using a Morlet wavelet of wavenumber 6, on the log (Extended Data Fig. 8b,d) and log(diff) data (Extended Data Fig. 9b,d). Strong signals are detected in the frequency bands between 2 and 7 years in all wavelet analyses. The signal power corresponding to the correlation strength of the mother wavelet is indicated by the colour coding (yellow: high; blue: low)⁵⁸. Signal powers below the $P = 0.05$ significance level above the null hypothesis of a red noise (lag = 0.9) are highlighted in red, and cones of influence (delimiting the regions with boundary effects) are superimposed in the lower corners of the plots. For further interpretations, we favour the log(diff) records (Extended Data Fig. 9b,d), which allow us to explore variability in the interannual range on unconstrained records where the autocorrelation effects were removed.

Numerical modelling

We used numerical simulations from several sources to estimate the changes in rainfall over NE Africa for the next century and during the NAHP. Simulations for end-of-the-century precipitation distribution (modelled ensemble mean precipitation) based on the sixth phase of the Coupled Model Intercomparison Model (CMIP6)⁵⁹ have been analysed to elucidate the spatial distribution of precipitation for different warming scenarios. We compared simulations for the shared socioeconomic pathways (SSP) 1.0–2.6 W m^{-2} (CMIP6-SSP126), 2.0–4.5 W m^{-2} (CMIP6-SSP245), 3.0–7.0 W m^{-2} (CMIP6-SSP370) and 5.0–8.5 W m^{-2} (CMIP6-SSP585) with the 1850–2010 baseline (CMIP6-Historical) (Extended Data Fig. 1 and Extended Data Table 1). These four scenarios vary between the low-end emission (‘taking the green road’, SSP126) and the high-end emission (‘taking the highway’, SSP585) scenarios^{60,61}. The scenario emissions are anticipated to produce a radiative forcing in 2100 of approximately 2.6 W m^{-2} in SSP126 due to an increasing shift towards sustainable practices, and 8.5 W m^{-2} in SSP585 due to a fossil-fuel-driven development. The mean seasonal precipitation (August–September–October) has been computed for the ensemble mean following four warming scenarios according to the SSP (Extended Data Fig. 1).

To determine whether the rainfall patterns during the NAHP can be used as analogues of predicted monsoon changes in warmer and wetter climates, we also used simulations performed using the AWI-ESM for climatologies at 9 kyr BP (9 K) to evaluate the rainfall dynamics over eastern Africa during the NAHP (Extended Data Fig. 2).

These simulations were performed using the boundary conditions as defined in ref. 62, with orbital parameters, greenhouse gases and ice sheets set at 9 K and an integration time of 800 years. The simulations depict an increase in summer rainfall in the monsoon region over North Africa (Extended Data Fig. 2a,b) and a Pacific Ocean configuration similar to a coastal El Niño^{39,44}. This untypical El Niño is characterized by a coastal warming in the eastern Pacific in otherwise basin-wide neutral or La Niña-type conditions and leads to sizeable rainfall in the Maritime Continent⁴⁴ (Extended Data Fig. 2c).

To test the reliability of the modelling experiment for estimating the rainfall dynamics at the Nile sources, we computed monthly means of daily precipitation in control runs for both the AWI-ESM and the CMIP6 ensemble and compared these with the observed annual rainfall cycle obtained from the Climatic Research Unit (CRU TS4) (Extended Data Fig. 3)⁶³. Both the AWI-ESM and the CMIP6 ensemble means capture well the seasonal rainfall dynamics but tend to underestimate rainfall in spring and autumn in the AWI-ESM and in summer in the CMIP6 ensemble mean (Extended Data Fig. 3a,b). The summer precipitation is largely enhanced in the 9 K simulation, whereas the CMIP6 ensemble mean shows a stronger rainfall anomaly at the end of the wet season (August–September) (Extended Data Fig. 3c–e). It is remarkable that the summer rainfall anomaly is very similar for the 9 K and for the warmest SSP585 scenario (Extended Data Fig. 3e). The cumulative annual rainfall falls in similar ranges for the simulations at 9 K and in all SSP scenarios (Extended Data Fig. 3d).

Data availability

The data presented here have been submitted to the Pangaea database (<https://pangaea.de/>) and are available at <https://doi.org/10.1594/PANGAEA.967743> (ref. 64) and <https://doi.org/10.1594/PANGAEA.967746> (ref. 65). The varve thickness and chronological data are accessible in the Varved Sediment Database (<https://varve.gfz-potsdam.de/database>).

References

- Halim, Y., Guergues, S. K. & Saleh, H. H. Hydrographic conditions and plankton in the South East Mediterranean during the last normal Nile flood (1964). *Int. Rev. Ges. Hydrobiol. Hydrogr.* **52**, 401–425 (1967).
- Heaton, T. J. et al. Marine20—the marine radiocarbon age calibration curve (0–55,000 cal BP). *Radiocarbon* **62**, 779–820 (2020).
- Blaauw, M. & Christen, J. A. Flexible paleoclimate age–depth models using an autoregressive gamma process. *Bayesian Anal.* **6**, 457–474 (2011).
- Jackson, B. et al. An algorithm for optimal partitioning of data on an interval. *IEEE Signal Process. Lett.* **12**, 105–108 (2005).
- Hammer, O., Harper, D. A. T. & Ryan, P. D. PAST: paleontological statistics software package for education and data analysis. *Palaeontol. Electron.* **4**, 9 (2001).
- Peltier, W. R., Argus, D. F. & Drummond, R. Space geodesy constrains ice age terminal deglaciation: the global ICE-6G_C (VM5a) model. *J. Geophys. Res. Solid Earth* **120**, 450–487 (2015).
- Ghil, M. et al. Advanced spectral methods for climatic time series. *Rev. Geophys.* **40**, 3–1–3–41 (2002).
- Torrence, C. & Compo, G. P. A practical guide to wavelet analysis. *Bull. Am. Meteorol. Soc.* **79**, 61–78 (1998).
- Eyring, V. et al. Overview of the Coupled Model Intercomparison Project Phase 6 (CMIP6) experimental design and organization. *Geosci. Model Dev.* **9**, 1937–1958 (2016).
- Riahi, K. et al. The shared socioeconomic pathways and their energy, land use, and greenhouse gas emissions implications: an overview. *Glob. Environ. Change* **42**, 153–168 (2017).
- O’Neill, B. C. et al. The roads ahead: narratives for shared socioeconomic pathways describing world futures in the 21st century. *Glob. Environ. Change* **42**, 169–180 (2017).

62. Shi, X., Lohmann, G., Sidorenko, D. & Yang, H. Early-Holocene simulations using different forcings and resolutions in AWI-ESM. *Holocene* **30**, 996–1015 (2020).
63. Harris, I., Osborn, T. J., Jones, P. & Lister, D. Version 4 of the CRU TS monthly high-resolution gridded multivariate climate dataset. *Sci. Data* **7**, 109 (2020).
64. Blanchet, C. L. et al. Annual flood-layer thickness of sediment core POS362-2_33 [dataset]. PANGAEA <https://doi.org/10.1594/PANGAEA.967743> (2024).
65. Blanchet, C. L. et al. Changepoints of annual flood-layer from sediment core POS362-2_33 [dataset]. PANGAEA <https://doi.org/10.1594/PANGAEA.967746> (2024).
66. Benjamin, D. J. et al. Redefine statistical significance. *Nat. Hum. Behav.* **2**, 6–10 (2018).
67. Laskar, J. et al. A long-term numerical solution for the insolation quantities of the Earth. *Astron. Astrophys.* **428**, 261–285 (2004).
68. Kobashi, T. et al. Volcanic influence on centennial to millennial Holocene Greenland temperature change. *Sci. Rep.* **7**, 1441 (2017).
69. Dix, M. et al. CSIRO-ARCCSS ACCESS-CM2 Model Output Prepared for CMIP6 CMIP Version 2 (Earth System Grid Federation, 2019); <https://doi.org/10.22033/ESGF/CMIP6.2281>
70. Ziehn, T. et al. CSIRO ACCESS-ESM1.5 Model Output Prepared for CMIP6 CMIP Version 1.5 (Earth System Grid Federation, 2019); <https://doi.org/10.22033/ESGF/CMIP6.2288>
71. Semmler, T. et al. AWI AWI-CM1.1MR Model Output Prepared for CMIP6 CMIP Version 1.1 (Earth System Grid Federation, 2018); <https://doi.org/10.22033/ESGF/CMIP6.359>
72. Swart, N. C. et al. CCCma CanESM5 Model Output Prepared for CMIP6 CMIP Version 5 (Earth System Grid Federation, 2019); <https://doi.org/10.22033/ESGF/CMIP6.1303>
73. EC-Earth-Consortium EC-Earth3 Model Output Prepared for CMIP6 CMIP (Earth System Grid Federation, 2019); <https://doi.org/10.22033/ESGF/CMIP6.181>
74. EC-Earth-Consortium EC-Earth3-Veg Model Output Prepared for CMIP6 CMIP (Earth System Grid Federation, 2019); <https://doi.org/10.22033/ESGF/CMIP6.642>
75. Krasting, J. P. et al. NOAA-GFDL GFDL-ESM4 Model Output Prepared for CMIP6 CMIP (Earth System Grid Federation, 2019); <https://doi.org/10.22033/ESGF/CMIP6.1407>
76. Volodin, E. et al. INM INM-CM4-8 Model Output Prepared for CMIP6 CMIP (Earth System Grid Federation, 2019); <https://doi.org/10.22033/ESGF/CMIP6.1422>
77. Volodin, E. et al. INM INM-CM5-0 Model Output Prepared for CMIP6 CMIP (Earth System Grid Federation, 2019); <https://doi.org/10.22033/ESGF/CMIP6.1423>
78. Boucher, O. et al. IPSL IPSL-CM6A-LR Model Output Prepared for CMIP6 CMIP (Earth System Grid Federation, 2018); <https://doi.org/10.22033/ESGF/CMIP6.1534>
79. Tatebe, H. & Watanabe, M. MIROC MIROC6 Model Output Prepared for CMIP6 CMIP (Earth System Grid Federation, 2018); <https://doi.org/10.22033/ESGF/CMIP6.881>
80. Jungclaus, J. et al. MPI-M MPIESM1.2-HR Model Output Prepared for CMIP6 CMIP (Earth System Grid Federation, 2019); <https://doi.org/10.22033/ESGF/CMIP6.741>
81. Wieners, K.-H. et al. MPI-M MPIESM1.2-LR Model Output Prepared for CMIP6 CMIP (Earth System Grid Federation, 2019); <https://doi.org/10.22033/ESGF/CMIP6.742>
82. Yukimoto, S. et al. MRI MRI-ESM2.0 Model Output Prepared for CMIP6 CMIP (Earth System Grid Federation, 2019); <https://doi.org/10.22033/ESGF/CMIP6.621>
83. Cao, J. & Wang, B. NUIST NESMv3 Model Output Prepared for CMIP6 CMIP (Earth System Grid Federation, 2019); <https://doi.org/10.22033/ESGF/CMIP6.2021>

Acknowledgements

We thank J. Mingram and B. Brademann for assistance with microscopy and preparation of samples, respectively. We also thank H. Braun and J. Moernaut for their help with measurements of grain-size distributions. Earlier versions of this work have been discussed with colleagues in conferences and seminars, whom we acknowledge collectively. We thank also X. Shi for making available the AWI-CM runs. C.L.B. acknowledges the GFZ Potsdam for funding her research through a reintegration grant (2018–2020). Further funding was provided to M.B., V.K., C.L.B., A.R. and A.B. by the German Climate Modeling Initiative PalMod funded by the German Ministry of Education and Research (Bundesministerium für Bildung und Forschung, FKZ 01LP1910A, 01LP1918A) and to R.T., M.I. and A.B. through the Helmholtz Association joint programme ‘Changing Earth—Sustaining our Future’ (PoF IV). M.I., C.L.B. and A.B. also acknowledge support from the Helmholtz Climate Initiative REKLIM.

Author contributions

The research was conceptualized by C.L.B., who performed the sampling, microfacies identification and varve counting. C.L.B., A.R. and R.T. performed the statistical and data analyses; A.R. also provided the Bayesian age modelling framework. L.L., C.L.B. and A.R. prepared and performed the grain-size analyses. M.I. designed and analysed the numerical model outputs. M.B. and V.K. provided GIA simulations as well as background knowledge on RSL changes. A.B. provided expertise on microfacies analyses and access to laboratory infrastructure and resources. C.L.B. wrote the original draft and all authors contributed to the revision of the paper.

Funding

Open access funding provided by Helmholtz-Zentrum Potsdam Deutsches GeoForschungsZentrum - GFZ.

Competing interests

The authors declare no competing interests.

Additional information

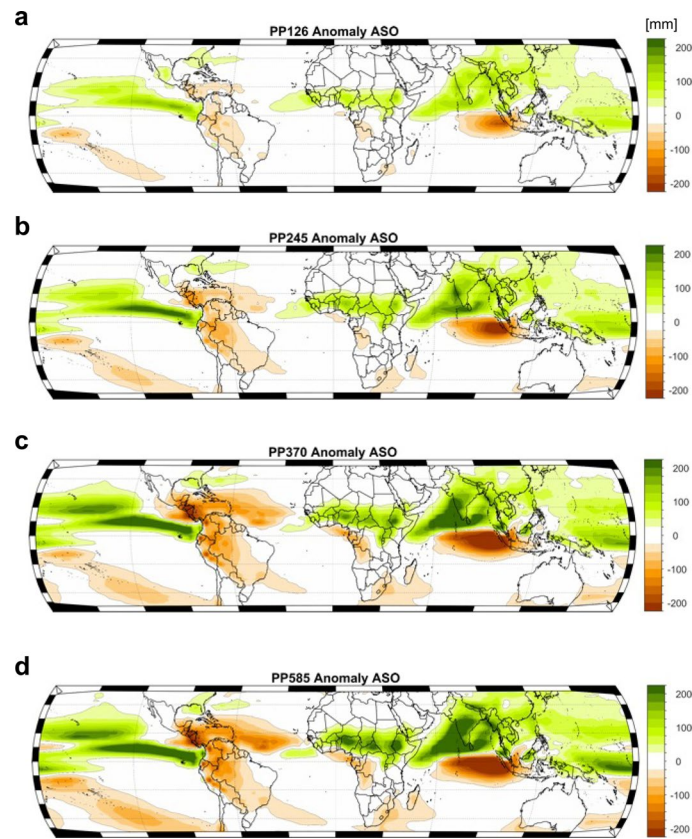
Extended data is available for this paper at <https://doi.org/10.1038/s41561-024-01471-9>.

Supplementary information The online version contains supplementary material available at <https://doi.org/10.1038/s41561-024-01471-9>.

Correspondence and requests for materials should be addressed to Cécile L. Blanchet.

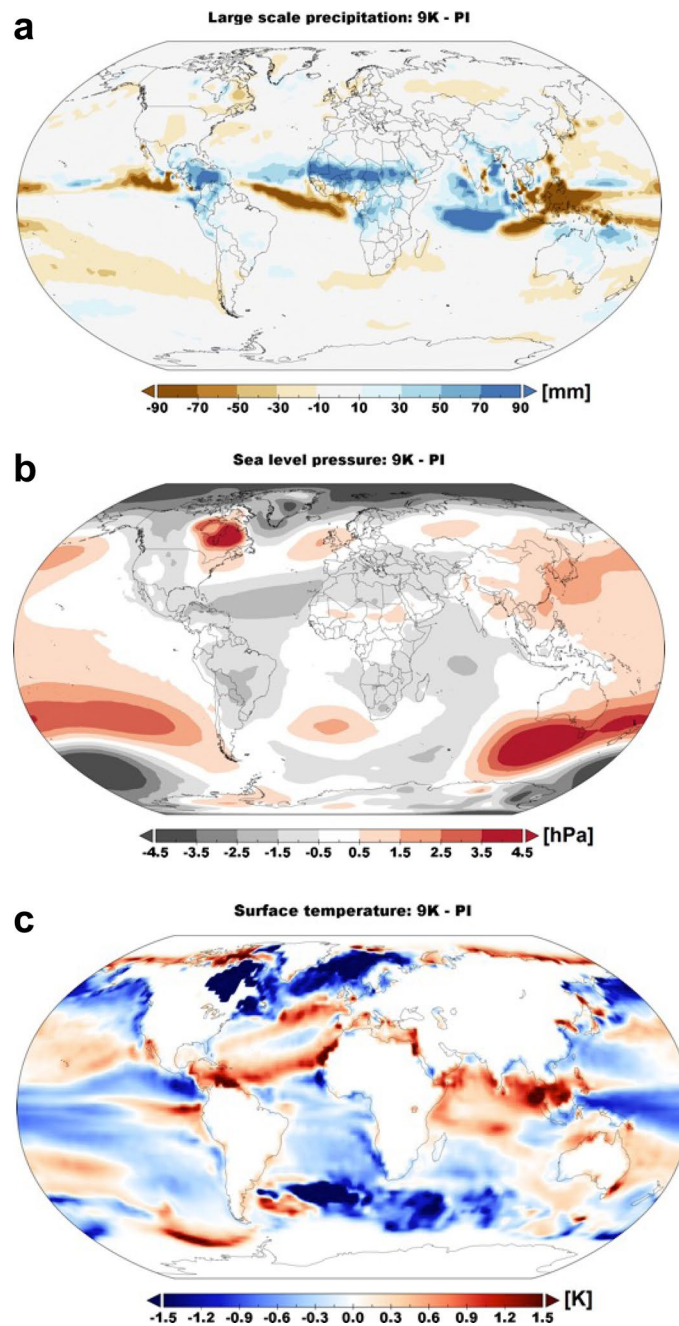
Peer review information *Nature Geoscience* thanks Mohamed Hamdan, Joseph Manning and Nick Marriner for their contribution to the peer review of this work. Primary Handling Editor: James Super and Alreza Bahadori, in collaboration with the *Nature Geoscience* team.

Reprints and permissions information is available at www.nature.com/reprints.



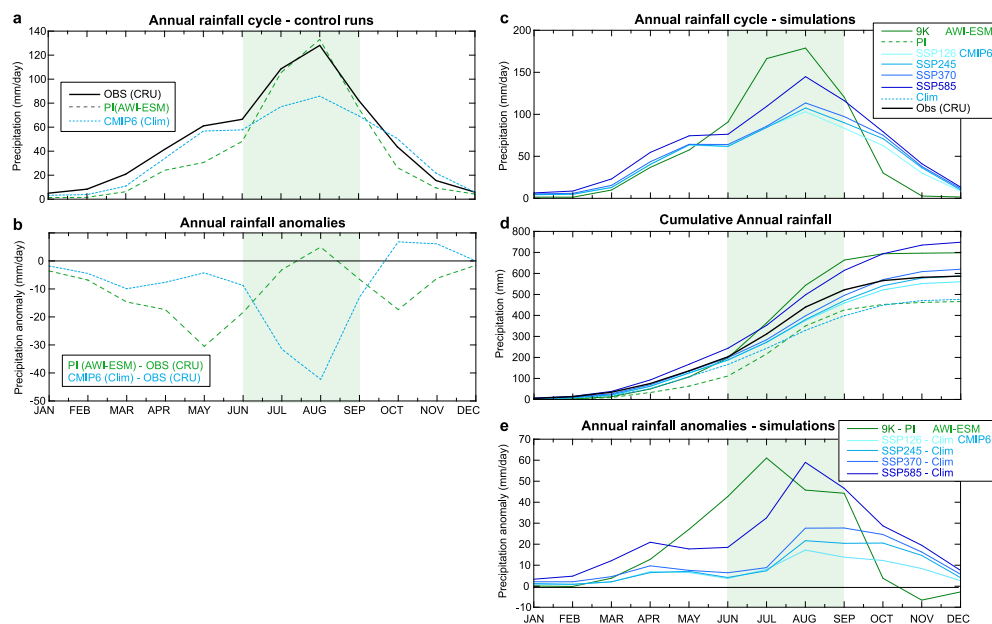
Extended Data Fig. 1 | Forecasted summer precipitation anomaly for different shared socio-economic pathways. Ensemble mean of August-September-October (ASO) precipitation anomaly over the period 2051–2100 relative to 1981–2010 based on Shared Socioeconomic Pathways.

a, SSP126, low-end emissions ('Taking the green road'). **b**, SSP245 intermediate emissions ('Middle of the road'). **c**, SSP370 regional rivalry ('A rocky road'). **d**, SSP585 high-end emissions ('Taking the highway'). A list with the models used to compute the ensemble mean can be found in Extended Table 1.



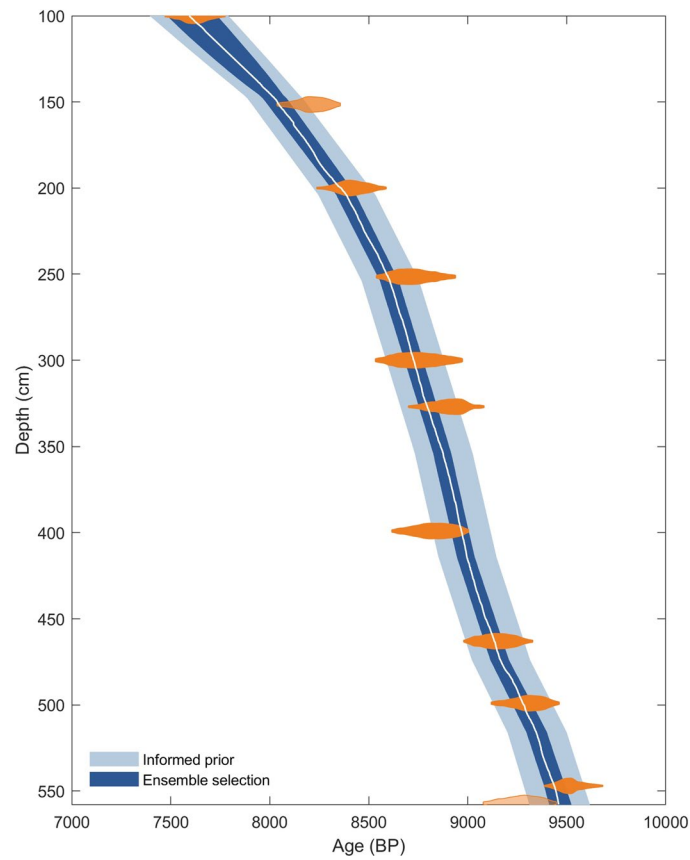
Extended Data Fig. 2 | Precipitation, sea-level pressure and sea-surface temperature during the Green Sahara (9 K). Ensemble mean of the August-September-October (ASO) anomalies during the Early Holocene (9 K)

relative to their corresponding control experiments (PI). **a**, Simulated large-scale precipitation anomalies. **b**, Sea-level pressure anomalies. **c**, Sea-surface temperature anomalies.



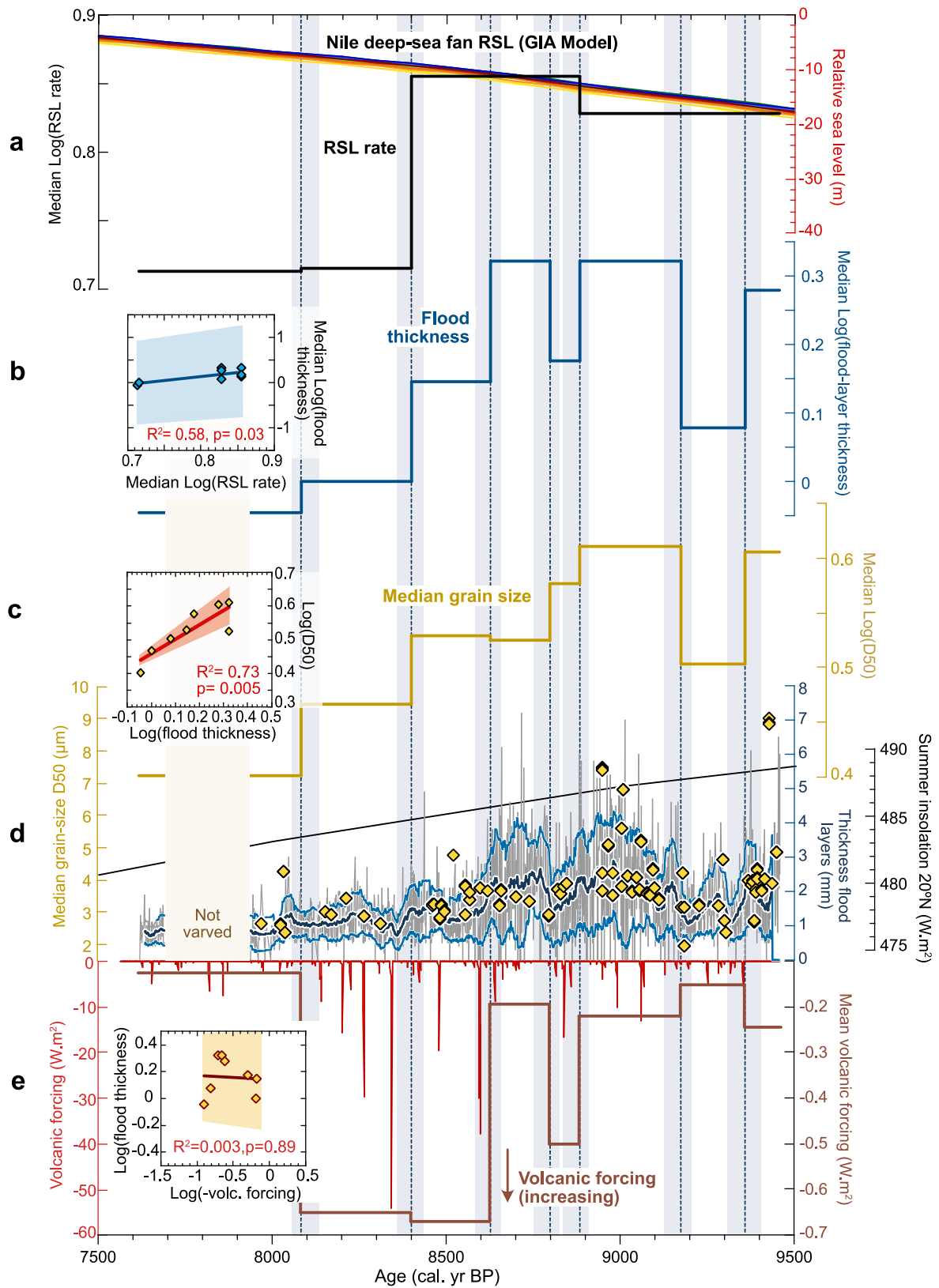
Extended Data Fig. 3 | Annual rainfall dynamics in CMIP6 mean ensemble and 9 K simulations of the AWI-ESM model as compared to observations (CRU) for the region 5–20°N, 25–45°E⁶³. **a**, Monthly mean of daily precipitation for the control runs, preindustrial (PI) for the AWI-ESM (green) and historical times (clim) for the CMIP6 ensemble mean (blue) and for the observation (CRU). **b**, monthly mean of daily rainfall anomalies between control runs and

observations. **c**, Monthly mean of daily precipitation for simulations at 9 K with AWI-ESM (green) and for several SSP scenarios in the CMIP6 ensemble mean (blue). **d**, Cumulative annual rainfall as in a and c. **e**, Monthly mean of daily precipitation between simulation and control runs, simulations at 9K-PI for the AWI-ESM (green) and between forecasts in the SSP scenarios-historical period (clim) in the CMIP6 ensemble mean (blue).



Extended Data Fig. 4 | Age-depth model for core P362/2-33. Orange violin distributions: radiocarbon ages measured on planktonic foraminifera *G. ruber*¹⁶ recalibrated using MARINE20⁵² (and no correction for reservoir age). The white curve is the accumulation rate profile from layer counting and thickness

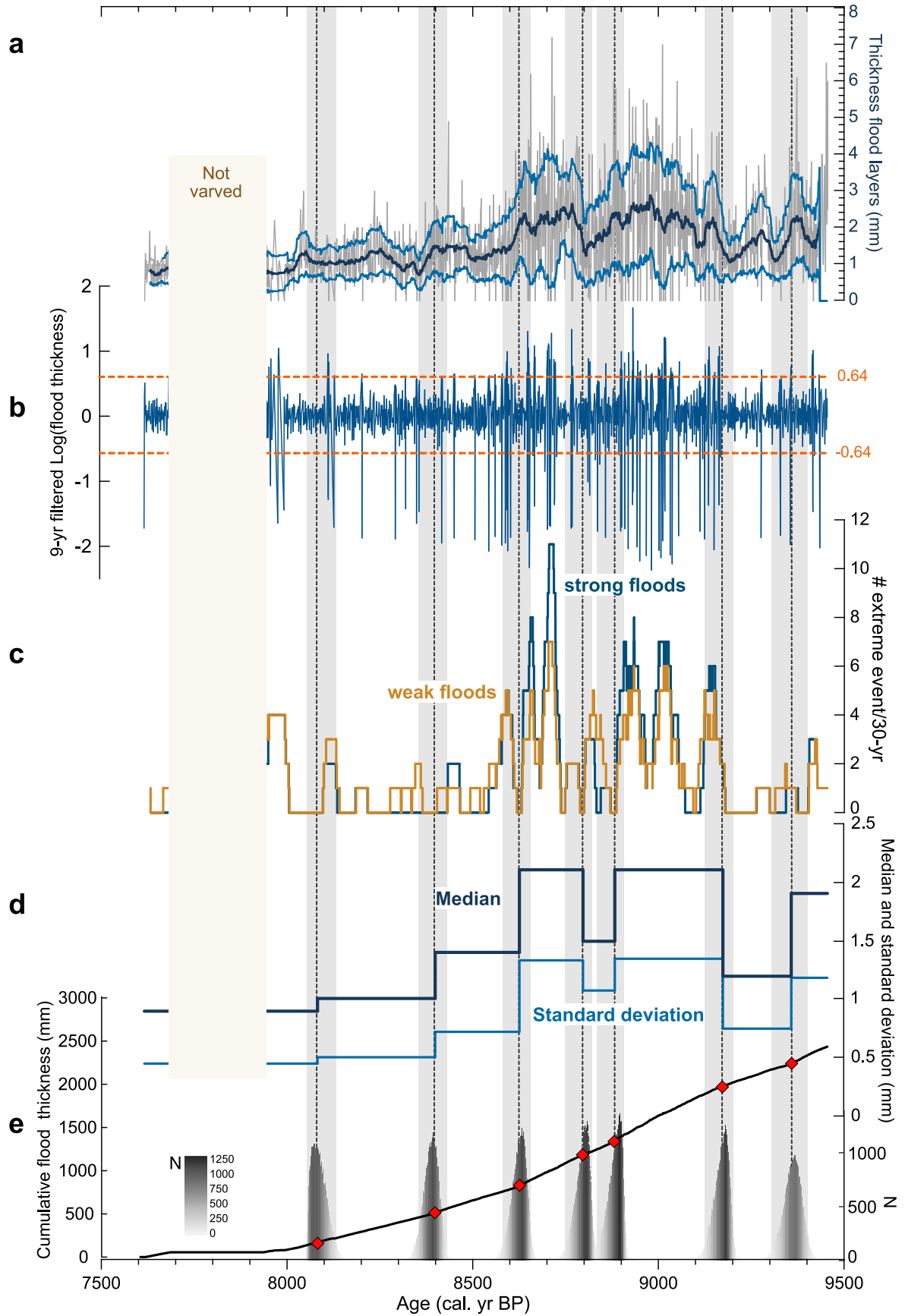
measurement tied to the youngest radiocarbon age, with 2-sigma uncertainty in light blue. Dark blue represents the Monte-Carlo for potential age-depth models respecting the age accumulation prior and radiocarbon dates.



Extended Data Fig. 5 | See next page for caption.

Extended Data Fig. 5 | Comparison of flood thickness with relative sea-level changes and grain-size distributions. **a**, Changes in relative sea-level (RSL) from the 3D glacial adjustment model (GIA) VILMA (see Methods) for different viscosity structures at the location of the Nile deep-sea fan (colour coding as in ref. 20). Changes in the rate of RSL between changepoints, calculated from ensemble mean of GIA simulations as median values of log-transformed RSL rate (black thick line) (see Methods). **b**, Median values of log-transformed flood-layer thickness between changepoints (blue thick line) and relationship between flood-layer thickness and RSL rates (bi-plot). The relationship between flood-layer thickness and RSL changes is considered non-significant since the calculated p-value of the null-hypothesis significance test is higher than 0.005⁶⁶ and the error around the regression are very large (blue shading). **c**, Averaged (median) values of median grain-sizes (D50) between changepoints (yellow thick line) calculated from (d) and relationship between flood-layer thickness

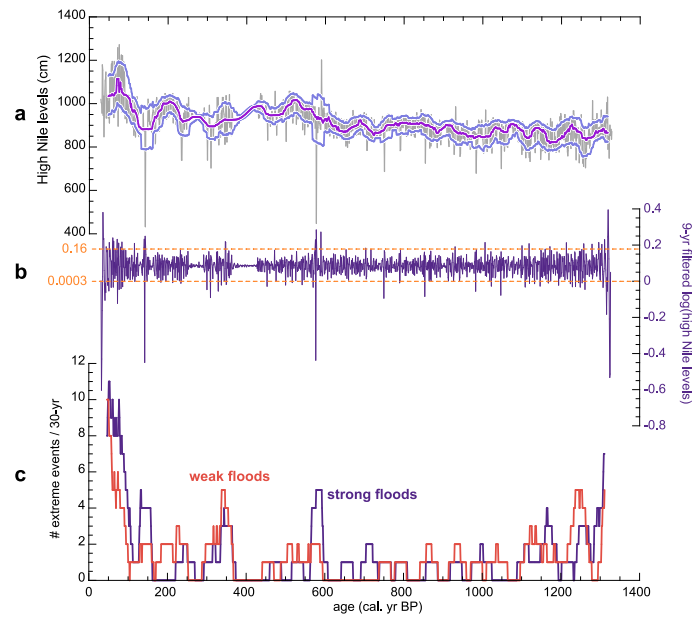
and median grain-size (bi-plot), which is considered significant since the calculated p-value of the null-hypothesis significance test is 0.005⁶⁶. **d**, Flood-layer thickness (grey) with the 30-yr moving median (dark blue) and the 1-sigma uncertainty (light blue). Median grain-sizes (D50) for 80 discrete samples (yellow diamonds). The relationship between flood-layer thickness and grain-size is considered significant since the p-value of the null-hypothesis significance test is equal to 0.005 and the error around the regression (orange shading) is small. Also shown the summer insolation at 20°N (black line)⁶⁷. **e**, Volcanic forcing reconstructed in GISP2 ice-core (red)⁶⁸ and mean volcanic forcing between tie-points (brown thick line). The relationship between volcanic forcing and flood-layer thickness is considered non-significant since the p-value is higher than 0.005. The location of changepoints (see Extended Data Fig. 5) is shown as dashed lines with uncertainties as grey bars.



Extended Data Fig. 6 | See next page for caption.

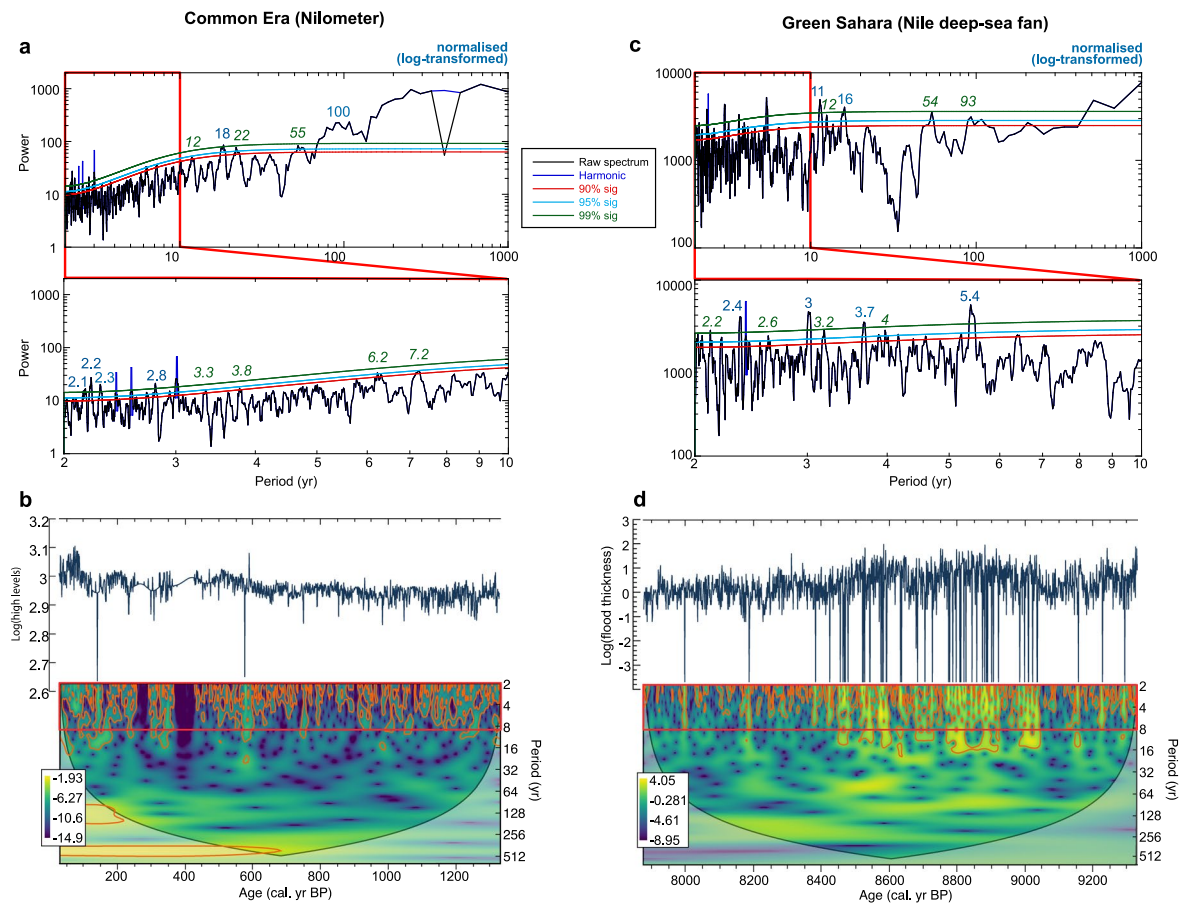
Extended Data Fig. 6 | Data analysis of the flood layer thickness of core P362/2-33. a, raw flood thickness (grey) with the 30-yr moving median (dark blue) and the 1-sigma uncertainty (light blue). **b**, logarithm of flood thickness, filtered with a high-pass 9-yr filter (dark grey) with 95 and 5 percentiles (orange dashed lines). **c**, number of extreme events per 30 yr moving window, with

highest floods (blue) and lowest floods (orange). **d**, Median (dark blue line) and standard deviation (light blue line) of flood thicknesses between each changepoint. **e**, Cumulative flood thickness (black line) and changepoints (red diamonds) shown as histograms (grey scale represents the number of models showing a changepoint at a certain age, N).



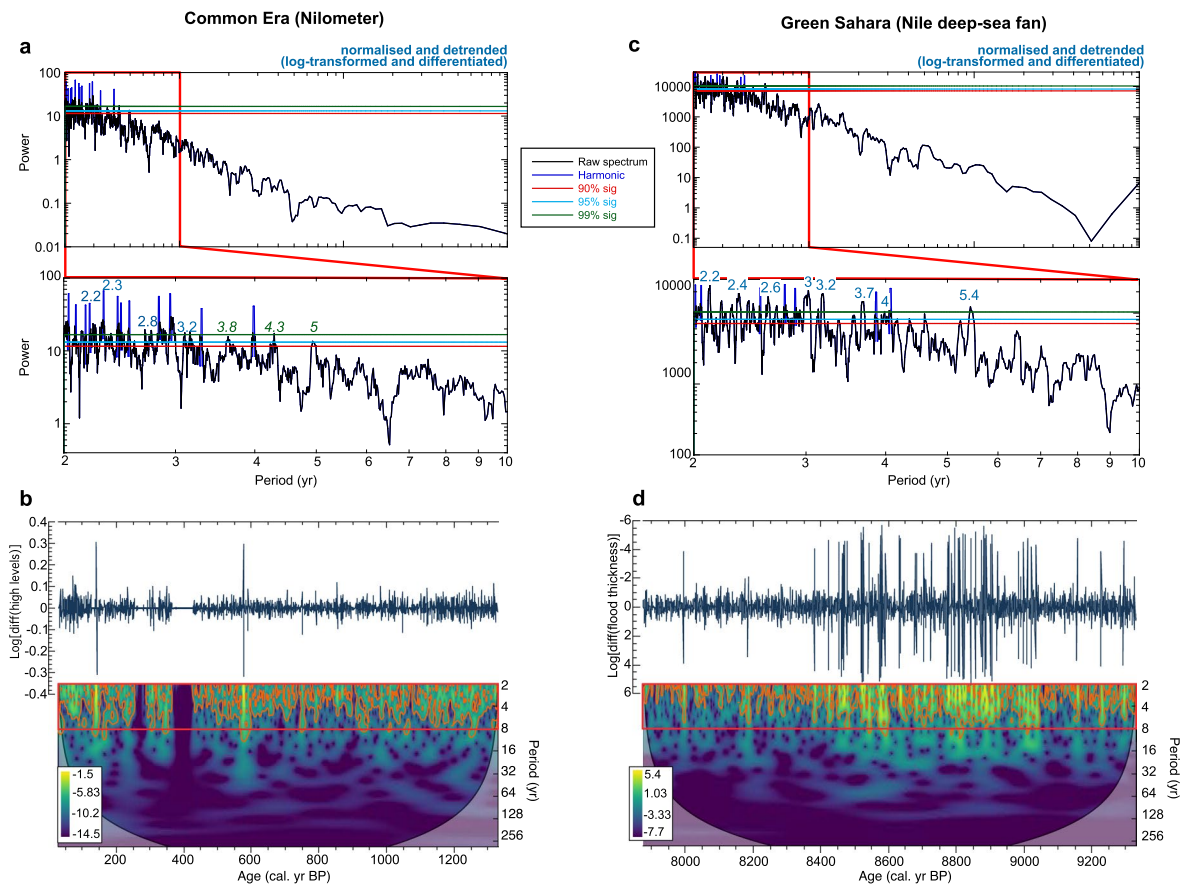
Extended Data Fig. 7 | Data analysis of high Nile levels from the Nilometers³¹. **a**, raw high Nile levels (grey) with the 30-yr moving median (dark purple) and the 1-sigma uncertainty (light purple). **b**, logarithm of high Nile levels, filtered with

a high-pass 9-yr filter (dark purple) with 95 and 5 percentiles (orange dashed lines). **c**, number of extreme events per 30-yr moving window, with highest floods (purple) and lowest floods (orange).



Extended Data Fig. 8 | Time-series analyses for the log-transformed Nilometer and Nile deep-sea fan records. **a**, Multi-taper analysis of the log-transformed high Nile level records during the Common Era (Nilometer data) with the periodogram (black), harmonics (blue) and significance levels against a red noise (90%: red; 95%: light blue; 99%: green). Red box: zoom on the 2–10 yr periodicity range. Significant frequencies above the 99% confidence level are indicated in blue, those above 95% in green italic. **b**, Plot of the log-transformed high Nile levels on the age scale (blue curve) and its continuous (Morlet) wavelet

transform with signal power indicated by the colour coding (left hand-side) and periodicities on the y-axis. Signal power is color-coded (yellow-blue for high-low) and powers above the $p = 0.05$ significance level above a red noise are shown as orange underlines. Cones of influence represent areas where periodicities are not significant and are superimposed in the lower corners of the plots. **c**, **d**, same as (a, b) for the log-transformed flood-layer thicknesses on the Nile deep-sea fan during the African Humid Period (this study).



Extended Data Fig. 9 | Time-series analyses for the log-transformed and differentiated Nilometer and Nile deep-sea fan records. **a**, Multi-taper analysis of the log-transformed and differentiated ($\log[x_t/x_{t+1}]$) high Nile level records during the Common Era (nilometer data) with the periodogram (black), harmonics (blue) and significance levels against a red noise (90%: red; 95%: light blue; 99%: green). Red box: zoom on the 2–10 yr periodicity range. Significant frequencies above the 99% confidence level are indicated in blue, and those above 95% in green italic. **b**, Plot of the log-transformed and differentiated high

Nile levels on the age scale (blue curve) and its continuous (Morlet) wavelet transform with signal power indicated by the colour coding (left hand-size) and periodicities on the y-axis. Signal power is color-coded (yellow-blue for high-low) and powers above the $p = 0.05$ significance level above a red noise are shown as orange underlines. Cones of influence represent areas where periodicities are not significant and are superimposed in the lower corners of the plots. **c**, **d**, same as (**a**, **b**) for the log-transformed and differentiated flood-layer thicknesses on the Nile deep-sea fan during the African Humid Period (this study).

Extended Data Table 1 | Models used in the CMIP6 experiment and their associated references

| Model name | Historical | SSP126 | SSP245 | SSP370 | SSP585 | Reference |
|---------------|---------------|---------------|---------------|---------------|---------------|-----------|
| ACCESS-CM2 | Precipitation | Precipitation | Precipitation | Precipitation | Precipitation | 67 |
| ACCESS-ESM1-5 | Precipitation | Precipitation | Precipitation | Precipitation | Precipitation | 68 |
| AWI-CM-1-1-MR | Precipitation | Precipitation | Precipitation | Precipitation | Precipitation | 69 |
| CanESM5 | Precipitation | Precipitation | Precipitation | Precipitation | Precipitation | 70 |
| EC-Earth3 | Precipitation | Precipitation | Precipitation | Precipitation | Precipitation | 71 |
| EC-Earth3-Veg | Precipitation | Precipitation | Precipitation | Precipitation | Precipitation | 72 |
| GFDL-ESM4 | Precipitation | Precipitation | Precipitation | Precipitation | Precipitation | 73 |
| INM-CM4-8 | Precipitation | Precipitation | Precipitation | Precipitation | Precipitation | 74 |
| INM-CM5-0 | Precipitation | Precipitation | Precipitation | Precipitation | Precipitation | 75 |
| IPSL-CM6A-LR | Precipitation | Precipitation | Precipitation | Precipitation | Precipitation | 76 |
| MIROC6 | Precipitation | Precipitation | Precipitation | Precipitation | Precipitation | 77 |
| MPI-ESM1-2-HR | Precipitation | Precipitation | Precipitation | Precipitation | Precipitation | 78 |
| MPI-ESM1-2-LR | Precipitation | Precipitation | Precipitation | Precipitation | Precipitation | 79 |
| MRI-ESM2-0 | Precipitation | Precipitation | Precipitation | Precipitation | Precipitation | 80 |
| NESM3 | Precipitation | Precipitation | Precipitation | Precipitation | Precipitation | 81 |

Data from refs. 69–83.